Progress In Electromagnetics Research M, Vol. 87, 93–102, 2019

Multistatic Airborne Passive Synthetic Aperture Radar Imaging Based on Two-Level Block Sparsity

Lele Qu* **and Yu Liu**

Abstract—Available multiple illuminators in a multistatic airborne passive synthetic aperture radar (SAR) system can enhance SAR imaging quality. In this paper, a new imaging algorithm based on two-level block sparsity for a multistatic airborne passive SAR system is proposed. The proposed imaging algorithm named by two-level block matching pursuit (BMP) algorithm utilizes both the spatially clustered property of observed targets and joint sparsity of the multistatic observation, i.e., two-level block sparsity to achieve the imaging reconstruction of an observed scene. The simulation results show that the proposed two-level BMP imaging algorithm for the multistatic airborne passive SAR system can reduce imaging reconstruction time and provide enhanced imaging reconstruction quality compared to the state-of-the-art structured sparse imaging algorithm.

1. INTRODUCTION

Passive radar which exploits an existing commercial transmitter as an illuminator of opportunity has proven to be a promising technology for target imaging, detection, and tracking [1]. Compared to a traditional active radar system, a passive radar system has the advantages of stealth operation, strong survivability, relative simplicity, and low cost. The available illuminators of opportunity include external sources include FM radio, Digital Video Broadcasting-Terrestrial (DVB-T), China Mobile Multimedia Broadcasting (CMMB), Global Navigation Satellite System (GNSS), and Wi-Fi signal [2–4]. While many passive radar systems are focused on the detection of targets with stationary ground-based receivers, the passive radar systems mounted on the moving airborne platform have received substantial attention in recent years [5–7]. Airborne passive synthetic aperture radar (SAR) can allow two-dimensional images of the ground surface to be imaged while providing the advantage of an increased target detection range and a reduced terrain masking effect [8–12].

Passive radar suffers from narrow signal bandwidth and low carrier frequency. As such, it is important to exploit multiple available illuminators for multistatic operation to enhance the imaging quality. The availability of multiple spatially separated illuminators of opportunity provides a way to achieve multistatic diversity and overall signal enhancement. In recent years, a sparsity-driven optimization technique based on compressive sensing has shown effectiveness in high-resolution passive radar imaging [13–16]. Two types of block sparsity properties are satisfied in a multistatic airborne passive SAR imaging scenario. Firstly, most targets extend over a set of pixels, and nonzero pixels of the reconstructed image occur in clusters. This clustering property of targets is referred to as block sparsity in the spatial domain. On the other hand, the reflection coefficients of underlying targets vary dependently for bistatic pairs associated with different illuminators. As a result, the locations of dominant pixels with nonzero values are common to all the images for different bistatic pairs, but the values of dominant pixels are different. This signal structure is called block sparsity in the observational dimensionality. In [17], a structured Bayesian compressive sensing (BCS) algorithm which utilizes two

Received 30 September 2019, Accepted 19 November 2019, Scheduled 12 December 2019
* Corresponding author: Lele Qu (lele83.qu@gmail.com).
The authors are with the College of Electronic Information Engineering, Shenyang Aerospace University, Shenyang 110136, China.

types of block sparsity introduced by a clustering target and multistatic observation has been proposed to deal with multistatic airborne passive SAR imaging. However, the structured BCS imaging algorithm has huge computational complexity, and there are some unknown parameters that need to be manually tuned, which is not practical to the multistatic airborne passive SAR imaging.

To solve the above problem, we develop a new multistatic airborne passive SAR imaging algorithm using a two-level block matching pursuit (BMP) technique in this paper. As a greedy algorithm, the two-level BMP method is computationally efficient and easy to implement in practice. Inspired by the work in [18], the proposed two-level BMP method combines the probabilistic graph model (PGM) [19, 20] and greedy pursuit framework [21] to describe the clustered characteristic of targets for each illuminator of opportunity and the joint sparsity property for all the illuminators of opportunity. The simulation results show that the proposed two-level BMP imaging algorithm for the multistatic airborne passive SAR system can reduce reconstruction time and provide enhanced imaging reconstruction quality.

The remainder of this paper is organized as follows. In Section 2, the signal model of multistatic airborne passive SAR system is formulated. The proposed two-level BMP imaging algorithm for the multistatic airborne passive SAR system is proposed in Section 3. Simulation experiments are provided in Section 4 to validate the proposed imaging approach. Conclusions are given in Section 5.

2. MULTISTATIC AIRBORNE PASSIVE SAR SIGNAL MODEL

Consider a multistatic airborne passive SAR system consisting of Q stationary illuminators of opportunity and a moving airborne receiver which flies along a linear trajectory Γ. It is supposed that Q transmitters of opportunity located at known stationary position $\mathbf{a}^{(q)}$ $(q = 1, 2, \ldots, Q)$ transmit waveforms in non-overlapping frequency bands which are respectively centered at $f^{(q)}$. At the nth $(n = 1, 2, \ldots, N)$ azimuth location of the moving airborne receiver $\mathbf{P}_n$, the direct path signal received from the qth $(q = 1, 2, \ldots, Q)$ transmitter is expressed as

$$d_n^{(q)}(t) = u^{(q)}\left(t - \tau_{dn}^{(q)}\right) \exp\left[j2\pi f^{(q)}\left(t - \tau_{dn}^{(q)}\right)\right] \tag{1}$$

where $u^{(q)}(t)$ is the complex envelope of the signal transmitted by the qth illuminator; $\tau_{dn}^{(q)} = R_{dn}^{(q)}/c$ is the time delay related to direct path signal; $R_{dn}^{(q)} = |\mathbf{a}^{(q)} - \mathbf{P}_n|$ represents the distance between the qth transmitter and the nth receiver position; c is the speed of wave propagation. It is assumed that the direct path signal transmitted from each illuminator is perfectly reconstructed at the receiver after demodulation and forward error correction.

For the qth illuminator, the surveillance signal reflected from the targets received at the nth azimuth location is given by

$$r_n^{(q)}(t) = \int \theta^{(q)}(\boldsymbol{\rho}, \mathbf{P}_n) u^{(q)}\left(t - \tau_{pn}^{(q)}(\boldsymbol{\rho})\right) \exp\left[j2\pi f^{(q)}\left(t - \tau_{pn}^{(q)}(\boldsymbol{\rho})\right)\right] d\boldsymbol{\rho} \tag{2}$$

where $\theta^{(q)}(\boldsymbol{\rho}, \mathbf{P}_n)$ is the reflection coefficient of target corresponding to the qth illuminator at the position $\boldsymbol{\rho}$ when the receiver is positioned at $\mathbf{P}_n$; $\tau_{pn}^{(q)}(\boldsymbol{\rho}) = R_{pn}^{(q)}/c$ is the bistatic time delay related to the qth illuminator; $R_{pn}^{(q)} = |\boldsymbol{\rho} - \mathbf{a}^{(q)}| + |\boldsymbol{\rho} - \mathbf{P}_n|$ is the bistatic range between the qth illuminator, the target, and the nth receiver position.

After demodulation, we perform a complex correlation operation on the baseband signals of direct path and surveillance channels and obtain

$$\begin{aligned} z_n^{(q)}(t) \;=\; & \int \theta^{(q)}(\boldsymbol{\rho}, \mathbf{P}_n) \left\{ u^{(q)}\left(t - \tau_{dn}^{(q)}\right) \exp\left(-j2\pi f^{(q)} \tau_{dn}^{(q)}\right) \right\} \\ & \otimes \left\{ u^{(q)}\left(t - \tau_{pn}^{(q)}(\boldsymbol{\rho})\right) \exp\left(-j2\pi f^{(q)} \tau_{pn}^{(q)}(\boldsymbol{\rho})\right) \right\} d\boldsymbol{\rho} \end{aligned} \tag{3}$$

where $\otimes$ denotes the complex correlation operation. $U^{(q)}(f)$ and $Z_n^{(q)}(f)$ are the Fourier transforms of $u^{(q)}(t)$ and $z_n^{(q)}(t)$, respectively. Then Eq. (3) can be transformed into the frequency domain as

$$Z_n^{(q)}(f) = \int \theta^{(q)}(\boldsymbol{\rho}, \mathbf{P}_n)[U^{(q)}(f)][U^{(q)}(f)]^* \exp\left[-j2\pi\left(f + f^{(q)}\right)\left(\tau_{pn}^{(q)}(\boldsymbol{\rho}) - \tau_{dn}^{(q)}\right)\right] d\boldsymbol{\rho} \tag{4}$$

where $f \in (-B^{(q)}/2, B^{(q)}/2)$, $B^{(q)}$ is the bandwidth of baseband signal of the qth illuminator. Defining the filter factor $G(f) = [U^{(q)}(f)][U^{(q)}(f)]^*$ and performing filtering operation in the frequency domain, Eq. (4) can be reformulated as

$$y_n^{(q)}(f) = \int \theta^{(q)}(\boldsymbol{\rho}, \mathbf{P}_n) \exp\left[-j2\pi\left(f + f^{(q)}\right)\left(\tau_{pn}^{(q)}(\boldsymbol{\rho}) - \tau_{dn}^{(q)}\right)\right] d\boldsymbol{\rho} \tag{5}$$

where $y_n^{(q)}(f) = Z_n^{(q)}(f)/G(f)$.

By discretizing the observed scene into $P_x \times P_y$ pixels, Eq. (5) can be represented as the matrix-vector form

$$\mathbf{y}_n^{(q)} = \boldsymbol{\Psi}_n^{(q)} \boldsymbol{\theta}^{(q)} + \boldsymbol{\varepsilon}_n^{(q)} \tag{6}$$

where $\boldsymbol{\theta}^{(q)}$ is the $P_x P_y \times 1$ scene reflectivity vector related to the qth bistatic pair; $\mathbf{y}_n^{(q)} = [y_n^{(q)}(f_1), y_n^{(q)}(f_2), \ldots, y_n^{(q)}(f_M)]^T$ is the $M \times 1$ frequency measurements collected at the nth azimuth position; $\boldsymbol{\varepsilon}_n^{(q)}$ is the $M \times 1$ noise vector which accounts for measurement noise; $\boldsymbol{\Psi}_n^{(q)}$ is the $M \times P_x P_y$ dictionary matrix; and the mth ($m = 1, 2, \ldots, M$) element of the lth ($l = 1, \ldots, P_x P_y$) column of $\boldsymbol{\Psi}_n^{(q)}$ is given by

$$[\boldsymbol{\Psi}_n^{(q)}]_{m,l} = \exp\left[-j2\pi\left(f_m + f^{(q)}\right)\left(\tau_{pn}^{(q)}(\boldsymbol{\rho}_l) - \tau_{dn}^{(q)}\right)\right] \tag{7}$$

where $\boldsymbol{\rho}_l$ is the spatial location vector representing the spatial location of the lth pixel.

Stacking the frequency measurements from all N azimuth locations, we have the following MMV problem

$$\mathbf{y}^{(q)} = \boldsymbol{\Psi}^{(q)} \boldsymbol{\theta}^{(q)} + \boldsymbol{\varepsilon}^{(q)} \tag{8}$$

where $\mathbf{y}^{(q)} = [\mathbf{y}_1^{(q)^T}, \ldots, \mathbf{y}_N^{(q)^T}]^T$, $\boldsymbol{\Psi}^{(q)} = [\boldsymbol{\Psi}_1^{(q)^T}, \ldots, \boldsymbol{\Psi}_N^{(q)^T}]^T$, and $\boldsymbol{\varepsilon}^{(q)} = [\boldsymbol{\varepsilon}_1^{(q)^T}, \ldots, \boldsymbol{\varepsilon}_N^{(q)^T}]^T$. It is noted that for each illuminator, $\boldsymbol{\theta}^{(q)}$ have a block sparsity feature due to the spatially clustering characteristics of observed targets. On the other hand, the non-zero reflection coefficients of targets have common support for multiple illuminators; however, their exact values are different. Thus, $\boldsymbol{\theta}^{(q)}$ have joint sparsity pattern for multiple illuminators. Therefore, $\boldsymbol{\theta}^{(q)}$ have two classes of structure block sparsity, and the multistatic airborne passive SAR imaging reconstruction can be formulated as the recovery of $\boldsymbol{\theta}^{(q)}$ with two-level block sparsity.

3. TWO-LEVEL BMP ALGORITHM

3.1. Probabilistic Graph Model

Firstly, we define the support set $\Lambda^{(q)}$ corresponding to target area as the set of indices corresponding to the dominant coefficients in $\boldsymbol{\theta}^{(q)}$. The complementary set of $\Lambda^{(q)}$ is $\bar{\Lambda}^{(q)}$, which is related to the artifact area in $\boldsymbol{\theta}^{(q)}$. The support area $\mathbf{s}$ is denoted by a vector composed of 1 and -1, where $\mathbf{s}_{\Lambda_{(q)}} = \mathbf{1}$ and $\mathbf{s}_{\bar{\Lambda}_{(q)}} = -\mathbf{1}$. The support area $\mathbf{s}$ can be described by the second-order Markov random field, where each pixel interacts only with its neighbors. The contribution of the interaction between a pixel and its neighbors can be described by

$$p(s_i|\mathbf{s}_{N_i}) = \exp\left(\sum_{i' \in N_i} s_i s_{i'}\right) / Z(\mathbf{s}_{N_i}) \tag{9}$$

where N_i is the set of all neighbors of pixel i, and $Z(\mathbf{s}_{N_i})$ is the normalizing function of the conditional probability density function (PDF).

Figure 1 shows the PGM model for describing the two-level block sparsity. The support vertex s_i is related to its neighbors $\mathbf{s}_{N_i}$ according to the cluster property. The value of s_i determines whether the values of $\{\theta_i^{(1)}, \theta_i^{(2)}, \ldots, \theta_i^{(Q)}\}$ are zero according to the joint sparsity pattern. By

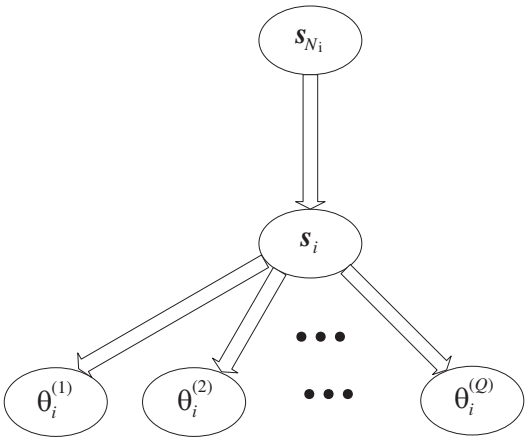

Figure 1. PGM model for describing the two-level block sparsity.

assuming the independence of the measurement data for different illuminators, the reflection coefficients $\theta_i^{(1)}, \theta_i^{(2)}, \ldots, \theta_i^{(Q)}$ are independent values, and their common support area is given by

$$p\left(\theta_i^{(1)}, \theta_i^{(2)}, \ldots, \theta_i^{(Q)} | s_i\right) = \prod_{q=1}^{Q} p\left(\theta_i^{(q)} | s_i\right) \tag{10}$$

It is noted that $\theta_i^{(q)}$ is the dominant nonzero coefficient with the high probability when $s_i = 1$. On the contrary, $\theta_i^{(q)}$ is the zero value with the high probability when $s_i = -1$. According to [22], the joint PDF of vertices in Fig. 1 is given by

$$p\left(\mathbf{s}_{N_i}, s_i, \theta_i^{(1)}, \ldots, \theta_i^{(Q)}\right) = p(\mathbf{s}_{N_i}) p(s_i | \mathbf{s}_{N_i}) \prod_{q=1}^{Q} p\left(\theta_i^{(q)} | s_i\right) \propto p\left(s_i | \mathbf{s}_{N_i}\right) \prod_{q=1}^{Q} p\left(\theta_i^{(q)} | s_i\right) = J(s_i) \tag{11}$$

where $J(s_i)$ is the function depends on s_i, and s_i is estimated by maximizing the joint PDF in Eq. (11) as follows

$$\hat{s}_i = \underset{s_i \in \{-1,1\}}{\arg\max}\ J(s_i) \tag{12}$$

It is worth mentioning that the value of s_i is determined by two factors in Eq. (12). By maximizing the first term $p(s_i|\mathbf{s}_{N_i})$, we can preserve the spatially clustered property of targets. The joint sparsity pattern is kept for all the measurement data for multiple illuminators of opportunity by maximizing the second term $\prod_{q=1}^{Q} p(\theta_i^{(q)}|s_i)$. The solution to Eq. (12) is given by

$$\begin{cases} \hat{s}_i = 1, & \text{when } \Delta > 0 \\ \hat{s}_i = -1, & \text{when } \Delta \leq 0 \end{cases} \tag{13}$$

where $\Delta = 2 \sum_{i' \in N_i} s_{i'} + \sum_{q=1}^{Q} \log[p(\theta_i^{(q)}|s_i = 1)/p(\theta_i^{(q)}|s_i = -1)]$.

The geometrical approximation [20] can be utilized to determine the PDFs $p(\theta_i^{(q)}|s_i = 1)$ and $p(\theta_i^{(q)}|s_i = -1)$. The geometrical approximation of PDFs is illustrated in Fig. 2. We can use the piece-constant function to determine the PDFs $p(\theta_i^{(q)}|s_i = 1)$ and $p(\theta_i^{(q)}|s_i = -1)$ as respectively illustrated in Figs. 2(a) and (b).

Accordingly, $p(\theta_i^{(q)}|s_i = 1)/p(\theta_i^{(q)}|s_i = -1)$ is determined by as shown in Fig. 2(c)

$$p\left(\theta_i^{(q)} | s_i = 1\right) / p\left(\theta_i^{(q)} | s_i = -1\right) = \begin{cases} \varepsilon_3/\varepsilon_2 & \left|\theta_i^{(q)}\right| \geq \tau \\ \varepsilon_4/\varepsilon_1 & \left|\theta_i^{(q)}\right| < \tau \end{cases} \tag{14}$$

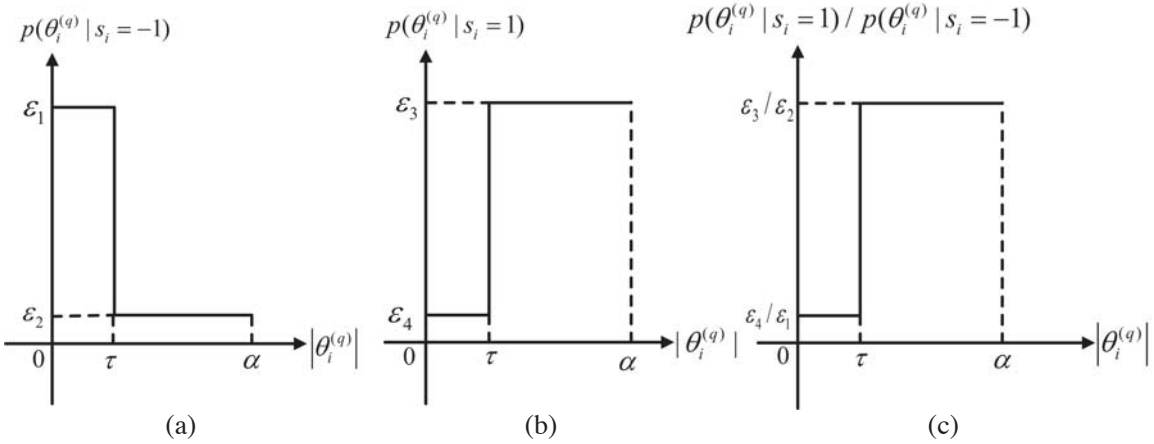

Figure 2. Geometrical approximation of PDFs.

where τ is the threshold value. We define the indicator function

$$I(x) = \begin{cases} 1 & |x| \geq \tau \\ 0 & |x| < \tau \end{cases} \tag{15}$$

Then we have

$$\Delta = 2 \sum_{i' \in N_i} s_{i'} + \sum_{q=1}^{Q} \log \left[\frac{\varepsilon_3}{\varepsilon_2} I\left(\theta_i^{(q)}\right) + \frac{\varepsilon_4}{\varepsilon_1} \left(1 - I\left(\theta_i^{(q)}\right)\right) \right] \tag{16}$$

Assuming that $\varepsilon_4/\varepsilon_1 = \delta$ and $\varepsilon_3/\varepsilon_2 = 1/\delta$ $(0 < \delta < 1)$, Eq. (16) can be reformulated as

$$\Delta = 2 \sum_{i' \in N_i} s_{i'} + \sum_{q=1}^{Q} \log \left[\frac{1}{\delta} I\left(\theta_i^{(q)}\right) + \delta \left(1 - I\left(\theta_i^{(q)}\right)\right) \right] \tag{17}$$

3.2. Two-Level BMP Algorithm

Two-level BMP algorithm uses PGM model to combine the multistatic illuminating group sparsity and spatially clustered sparsity, i.e., the two-level block sparsity to achieve imaging reconstruction. Before the introduction of two-level BMP algorithm, we first predefine three functions as follows.

(1) $\max\_\text{ind}(\mathbf{x}, K) \triangleq \{\text{the set of indices corresponding to the } K \text{ largest amplitude components } of\ \mathbf{x}\}$

(2) add $(\mathbf{x}, \Lambda) \triangleq \{\forall \in \Lambda,\ \text{perform}\ \ x_i = x_i + 1\}$

(3) $\Lambda_{vote} = \text{majority} - \text{vote}(\{\Lambda^{(q)} | q = 1, 2, \ldots, Q\})$: (a) Set $\mathbf{n} = \mathbf{0}^{P_x P_y \times 1}$; (b) $\mathbf{n} = add(\mathbf{n}, \Lambda^{(q)})$ for $q = 1, 2, \ldots, Q$; (c) $\Lambda_{vote} = \max\_ind(\mathbf{n}, K)$.

The detailed procedures of the two-level BMP algorithm are summarized in Table 1.

It is worth mentioning that the proposed two-level BMP algorithm requires the sparsity level K of observed scene as a part of its input to achieve an accurate imaging reconstruction. The sparsity level can be determined by running the two-level BMP algorithm within a range of sparsity level, which leads to an increase of computational cost of the proposed algorithm. If the change of the recover error is no longer significant with the increase of the value of K, the current value of K can be used as the input parameter of the proposed two-level BMP algorithm. The cross validation technique [23, 24] can also be an alternative way to estimate the appropriate sparsity level of observed scene.

Table 1. The detailed procedures of the two-level BMP algorithm.

Input: $\{\mathbf{y}^{(q)}, \mathbf{\Psi}^{(q)} | q = 1, 2, \ldots, Q\}$, the sparsity level K, $\{\varepsilon_1, \varepsilon_2, \varepsilon_3, \varepsilon_4\}$.
Initialization: $\mathbf{r}^{(q,old)} = \mathbf{y}^{(q)}$ for $q = 1, 2, \ldots, Q$; $\hat{\boldsymbol{\theta}}^{(q,old)} = \mathbf{0}^{P_x P_y \times 1}$ for $q = 1, 2, \ldots, Q$; $\mathbf{s} = -\mathbf{1}^{P_x P_y \times 1}$.
Repeat:

1. $\breve{\boldsymbol{\theta}}^{(q)} = (\mathbf{\Psi}^{(q)})^H \mathbf{r}^{(q,old)} + \hat{\boldsymbol{\theta}}^{(q,old)}$ for $q = 1, 2, \ldots, Q$.
2. $\Lambda^{(q)} = \text{max\_ind}(\breve{\boldsymbol{\theta}}^{(q)}, K)$ for $q = 1, 2, \ldots, Q$.
3. $\Lambda_{vote} = \text{majority} - \text{vote}(\{\Lambda^{(q)} | q = 1, 2, \ldots, Q\})$, then set $\mathbf{s}_{\Lambda_{vote}} = \mathbf{1}$, $\mathbf{s}_{\bar{\Lambda}_{vote}} = -\mathbf{1}$.
4. For each $i \in \{1, 2, \ldots, P_x P_y\}$, compute (16) by utilizing $\{\breve{\theta}_i^{(1)}, \breve{\theta}_i^{(2)}, \ldots, \breve{\theta}_i^{(Q)}\}$and $\mathbf{s}_{N_i}$; if $\Delta > 0$, $\hat{s}_i = 1$, else $\hat{s}_i = -1$.
5. $\Lambda_{esti} = \{$the set of indices which correspond to the locations of '1' in $\hat{\mathbf{s}}\}$.
6. $\hat{\boldsymbol{\theta}}^{(q,new)}_{\Lambda_{esti}} = (\mathbf{\Psi}^{(q)}_{\Lambda_{esti}})^{+} \mathbf{y}^{(q)}$, then the smallest $P_x P_y - K$ coefficients of $\hat{\theta}^{(q,new)}$ are set to be zeros for $q = 1, 2, \ldots, Q$.
7. $\mathbf{r}^{(q,new)} = \mathbf{y}^{(q)} - \mathbf{\Psi}^{(q)} \hat{\boldsymbol{\theta}}^{(q,new)}$ for $q = 1, 2, \ldots, Q$.
8. **If** $\sum_{q=1}^{Q} ||\mathbf{r}^{(q,old)}||_2^2 > \sum_{q=1}^{Q} ||\mathbf{r}^{(q,new)}||_2^2$, **then** $\mathbf{r}^{(q,old)} = \mathbf{r}^{(q,new)}$, $\hat{\boldsymbol{\theta}}^{(q,old)} = \hat{\boldsymbol{\theta}}^{(q,new)}$, return to step 1.

   Else
   Stop the iteration.
   End if

Output: $\sum_{q=1}^{Q} |\hat{\boldsymbol{\theta}}^{(q,old)}|$

4. SIMULATION EXPERIMENTS AND ANALYSIS

In this section, we evaluate the performance of the proposed two-level BMP algorithm for the multistatic airborne passive SAR system using synthetic data. The simulation scene is illustrated in Fig. 3. The Chinese mobile multimedia broadcast signal (CMMB) [2] whose bandwidth is 8 MHz is used as the transmission signal of opportunity. The positions of three illuminator are respectively $(5, -5, 6)$ km, $(5, 5, 6)$ km, and $(8, 0, 6)$ km. The initial position of the airborne passive SAR receiver is $[8, -1.2, 6]$ km, and it flies along a linear trajectory with a height of 6 km and a constant velocity of $[200, 0, 0]$ m/s. The observed scene to be imaged is chosen to be 96 m $\times$ 96 m and discretized into 16×16 pixels. We consider two squared continuous targets in the scene. Each target is composed of four pixels. Due to the illumination of multiple transmitters, it is assumed that the complex reflection coefficients of targets are assumed invariant for each transmitter whereas they vary for different transmitters due to the distinct aspect angles. The complex reflection coefficients of each target corresponding to three illuminators are set to $0.1 + 0.1$j, $0.2 + 0.2$j, and $0.3 + 0.3$j, respectively. Gaussian white noise is added to the received signal with a signal-to-noise ratio (SNR) of 25 dB. There are 60 azimuth positions along the flight trajectory, and the azimuthal sampling frequency is 5 Hz. At each azimuth location, a total of 21 frequency samples within 8 MHz bandwidth for each illuminator are utilized for imaging reconstruction.

The imaging result of the proposed two-level BMP algorithm is compared with that of the structured BCS algorithm in Fig. 4. The images in Fig. 4 are normalized to their own maxima and shown on $[-20\ 0]$ dB scale. It is observed from Fig. 4(b) that the proposed two-level BMP algorithm can accurately recover the continuous structure of two targets. However, it is shown in Fig. 4(c) that the structured BCS algorithm is unable to preserve the clustered structure of two targets with many spurious pixels.

In order to quantitatively evaluate the imaging reconstruction performance of two algorithms, the

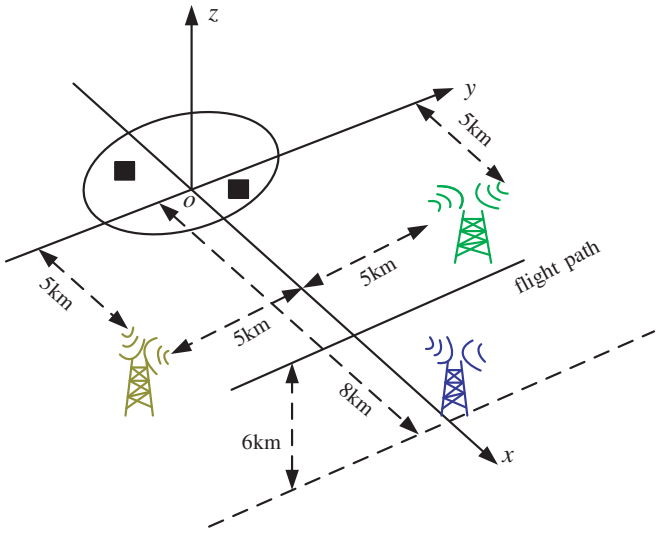

Figure 3. Geometry of multistatic airborne passive SAR system.

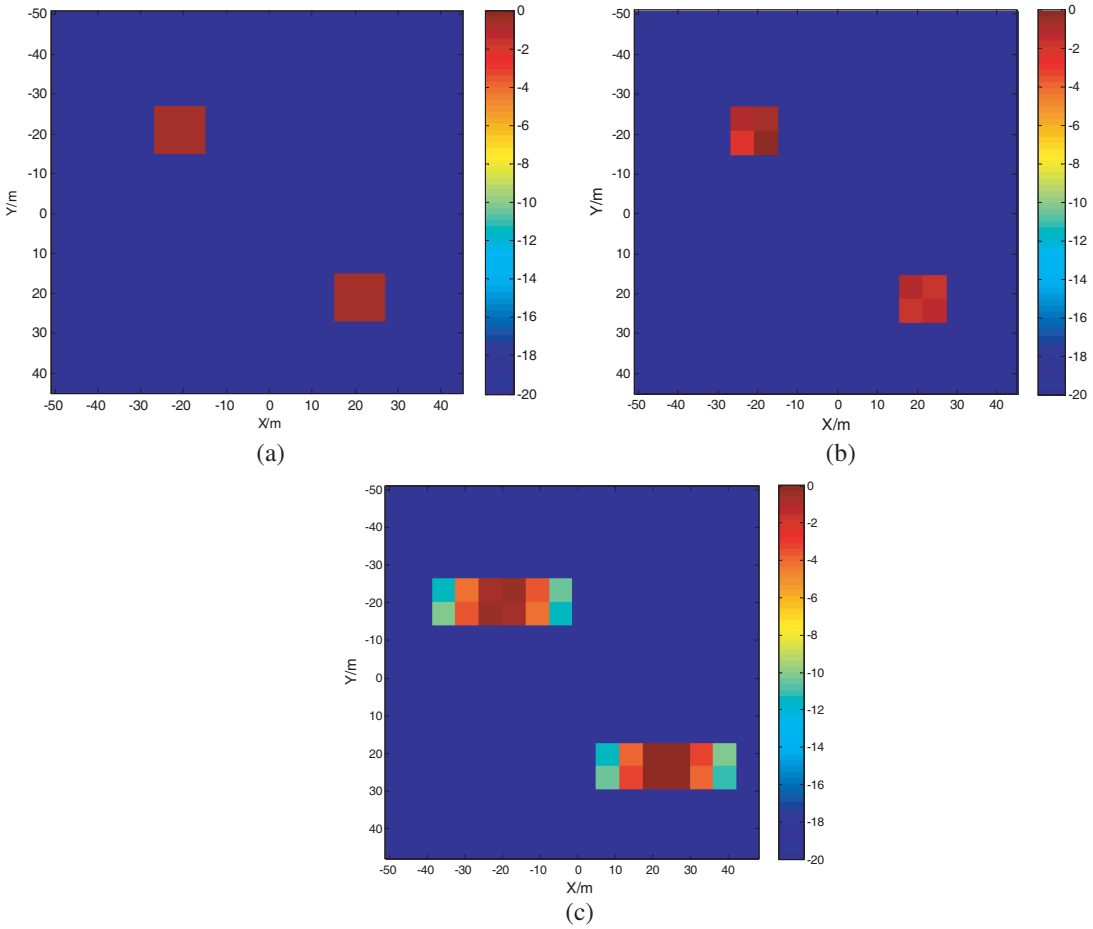

Figure 4. The original scene and corresponding imaging results. (a) Normalized magnitude of fused reflection coefficients of the original scene. (b) Image obtained by the proposed two-level BMP algorithm. (c) Image obtained by the structured BCS algorithm.

target-to-clutter ratio (TCR) [25] is adopted to measure the imaging performance. The definition of TCR is given by

$$\mathrm{TCR} = 10\lg \frac{(1/N_B)\sum_{(x,y)\in B}|I(x,y)|^2}{(1/N_C)\sum_{(x,y)\in C}|I(x,y)|^2} \tag{18}$$

where B is the target area, N_B the number of pixels in the target area B, C the non-target area, N_C the number of pixels in the non-target area C, and $I(x,y)$ the pixel value corresponding to the pixel in the image (x,y).

In order to evaluate the robustness of the proposed approach in the noisy environment, the reconstructed images are obtained by varying the SNR levels. Fig. 5 illustrates the TCR versus different SNR levels. The average TCR is calculated over 30 Monte Carlo runs for each noise level. It is shown from Fig. 5 that the proposed two-level BMP algorithm outperforms structured BCS algorithm in terms of TCR, which implies that the two-level BMP algorithm has better performance in recovering the clustered dominant pixels and suppressing the artificial pixels.

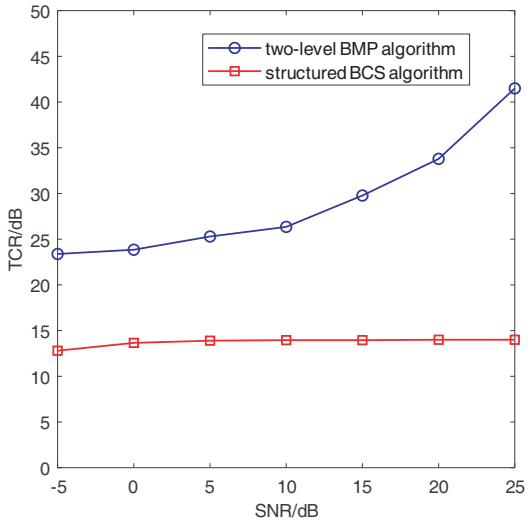

Figure 5. Average TCR comparison as a function of SNR.

Table 2 lists the computation complexity and computation time of two imaging algorithms. The computation complexity of two-level BMP algorithm is $O(K(P_xP_y + K^2)MNQ)$, whereas the computation complexity of structured BCS algorithm is $O(T(P_xP_y)^3)$, where T is the number of iterations of Markov Chain Monte Carlo (MCMC) sampling. The computational platform is a personal computer with the configuration of 8 GB random access memory, I5-3470 central processing unit, and a MATLAB (R2014a) environment. It can be found that the computation time of the proposed two-level BMP algorithm is dramatically less than that of the structured BCS algorithm. By utilizing the greedy pursuit framework, the two-level BMP algorithm is more computationally efficient than the structured BCS algorithm.

Table 2. Comparison of the computation complexity and time.

Algorithms	Computation complexity	Computation time(s)
Proposed two-level BMP algorithm	$O(K(P_xP_y + K^2)MNQ)$	0.467
Structured BCS algorithm	$O(T(P_xP_y)^3)$	74.387

5. CONCLUSION

In this paper, we have proposed a two-level BMP imaging algorithm for a multistatic passive airborne passive SAR system. The proposed two-level BMP imaging algorithm exploits the underlying target clustered structure and joint sparsity pattern in the context of multistatic airborne passive SAR system. The proposed two-level BMP imaging algorithm which allows the effective consideration of illuminator-dependent reflection coefficients of the spatially clustered targets exploits the PGM and greedy pursuit framework to implement the imaging reconstruction. Compared to the state-of-the-art structure-aware BCS algorithm, the proposed imaging algorithm provides enhanced imaging quality with higher TCR and less computation time.

ACKNOWLEDGMENT

This work was supported in part by the National Natural Science Foundation of China under Grant 61671310, in part by the Aeronautical Science Foundation of China under Grant 2016ZC54013, in part by the Innovative Talents Program of Universities of Liaoning Province under Grant LR2016062, in part by the Scientific Research Project of the Department of Education of Liaoning Province under Grants L201752 and L201744, in part by the Young and Middle-aged Science and Technology Innovation Talents Support Project of Shenyang City under Grant RC180038 and in part by Liaoning BaiQianWan Talents Program.

REFERENCES

1. Yonel, B., E. Mason, and B. Yazıcı, "Deep learning for passive synthetic aperture radar," *IEEE J. Sel. Topics Signal Process.*, Vol. 12, No. 1, 90–103, Feb. 2018.
2. Wan, X., J. Yi, Z. Zhao, and H. Ke, "Experimental research for CMMB-based passive radar under a multipath environment," *IEEE Trans. Aerosp. Electron. Syst.*, Vol. 50, No. 1, 70–85, Jan. 2014.
3. Liu, F., M. Antoniou, Z. Zeng, and M. Cherniakov, "Coherent change detection using passive GNSS-based BSAR: experimental proof of concept," *IEEE Trans. Geosci. Remote Sens.*, Vol. 51, No. 8, 4544–4555, Aug. 2013.
4. Pastina, D., et al., "Maritime moving target long time integration for GNSS-based passive bistatic radar," *IEEE Trans. Aerosp. Electron. Syst.*, Vol. 54, No. 6, 3060–3083, Dec. 2018.
5. Tan, D. K. P., M. Lesturgie, H. Sun, and Y. Lu, "Space-time interference analysis and suppression for airborne passive radar using transmissions of opportunity," *IET Radar, Sonar and Navigation*, Vol. 8, No. 2, 142–152, Feb. 2014.
6. Deng, Y., J. Wang, Z. Luo, and S. Guo, "Cascaded suppression method for airborne passive radar with contaminated reference signal," *IEEE Access*, Vol. 7, 50317–50329, 2019.
7. Yang, P., X. L. Yu, Z. Chai, D. Zhang, Q. Yue, and J. Yang, "Clutter cancellation along the clutter ridge for airborne passive radar," *IEEE Geosci. Remote Sens. Lett.*, Vol. 14, No. 6, 951–955, Jun. 2017.
8. Berthillot, C., A. Santori, O. Rabaste, D. Poullin, and M. Lesturgie, "BEM reference signal estimation for an airborne passive radar antenna array," *IEEE Trans. Aerosp. Electron. Syst.*, Vol. 53, No. 6, 2833–2845, Dec. 2017.
9. Wang, L., C. E. Yarman, and B. Yazici, "Doppler-Hitchhiker: A novel passive synthetic aperture radar using ultranarrowband sources of opportunity," *IEEE Trans. Geosci. Remote Sens.*, Vol. 49, No. 10, 3521–3537, Oct. 2011.
10. Dawidowicz, B., K. S. Kulpa, M. Malanowski, J. Misiurewicz, P. Samczynski, and M. Smolarczyk, "DPCA detection of moving targets in airborne passive radar," *IEEE Trans. Aerosp. Electron. Syst.*, Vol. 48, No. 2, 1347–1357, Apr. 2012.
11. Gromek, D., K. Kulpa, and P. Samczyński, "Experimental results of passive SAR imaging using DVB-T illuminators of opportunity," *IEEE Geosci. Remote Sens. Lett.*, Vol. 13, No. 8, 1124–1128, Aug. 2016.

12. Gromek, D., K. Radecki, J. Drozdowicz, P. Samczyński, and J. Szabatin, "Passive SAR imaging using DVB-T illumination for airborne applications," *IET Radar, Sonar and Navigation*, Vol. 13, No. 2, 213–221, Feb. 2019.
13. Liu, C. C. and W. D. Chen, "Sparse self-calibration imaging via iterative MAP in FM-based distributed passive radar," *IEEE Geosci. Remote Sens. Lett.*, Vol. 10, No. 3, 538–542, Oct. 2013.
14. Qiu, W., et al., "Compressive sensing-based algorithm for passive bistatic ISAR with DVB-T signals," *IEEE Trans. Aerosp. Electron. Syst.*, Vol. 51, No. 3, 2166–2180, Jul. 2015.
15. Yu, X. F., T. Y. Wang, X. F. Lu, C. Chen, and W. D. Chen, "Sparse passive radar imaging based on DVB-S using the Laplace-SLIM algorithm," *2014 International Radar Conference*, 1–4, Lille, 2014.
16. Zhang, Y. D., M. G. Amin, and B. Himed, "Structure-aware sparse reconstruction and applications to passive multistatic radar," *IEEE Aerosp. Electron. Syst. Mag.*, Vol. 32, No. 2, 68–78, Feb. 2017.
17. Wu, Q., Y. D. Zhang, M. G. Amin, and B. Himed, "High-resolution passive SAR imaging exploiting structured Bayesian compressive sensing," *IEEE J. Sel. Topics Signal Process.*, Vol. 9, No. 8, 1484–1497, Dec. 2015.
18. Wang, X., G. Li, Y. Liu, and M. G. Amin, "Two-level block matching pursuit for polarimetric through-wall radar imaging," *IEEE Trans. Geosci. Remote Sens.*, Vol. 56, No. 3, 1533–1545, Mar. 2018.
19. Cevher, V., P. Indyk, L. Carin, and R. G. Baraniuk, "Sparse signal recovery and acquisition with graphical models," *IEEE Signal Process. Mag.*, Vol. 27, No. 6, 92–103, Nov. 2010.
20. Cevher, V., M. F. Duarte, C. Hegde, and R. G. Baraniuk, "Sparse signal recovery using Markov random fields," *Proc. Adv. Neural. Inf.*, 257–264, 2009.
21. Tropp, J. A., A. C. Gilbert, and M. J. Strauss, "Algorithms for simultaneous sparse approximation. Part I: Greedy pursuit?," *Signal Process.*, Vol. 86, No. 3, 572–588, Mar. 2006.
22. Koller, D. and N. Friedman, *Probabilistic Graphical Models-Principles and Techniques*, MIT Press, Cambridge, MA, USA, 2009.
23. Ward, R., "Compressed sensing with cross validation," *IEEE Trans. on Inf. Theory*, Vol. 55, No. 12, 5773–5782, Dec. 2009.
24. Zhang, J., L. Chen, P. T. Boufounos, and Y. Gu, "On the theoretical analysis of cross validation in compressive sensing," *Proceeding of the 2014 IEEE International Conference on Acoustic, Speech, and Signal Processing, ICASSP 2014*, 3370–3374, Italy, 2014.
25. Seng, C. H., A. Bouzerdoum, M. G. Amin, and S. L. Phung, "Probabilistic fuzzy image fusion approach for radar through wall sensing," *IEEE Trans. Image Process.*, Vol. 22, No. 12, 4938–4951, Dec. 2013.